

Electronic Supporting Information

Upgrading well plates using open-microfluidic patterning

Samuel B. Berry^{*a}, Tianzi Zhang^{*a}, John H. Day^a, Xiaojing Su^a, Ilham Z. Wilson^a, Erwin Berthier^a, Ashleigh B. Theberge^{a,b,y}

^aDepartment of Chemistry, University of Washington, Seattle, Washington 98195, USA,

^bDepartment of Urology, University of Washington School of Medicine, Seattle, Washington 98195, USA

^{*}these authors contributed equally to this work.

^ycorresponding author: abt1@uw.edu

Table of Contents:

Figure S-1: Illustrations of radii of curvature for calculation of Laplace pressure in our system

Figure S-2: Heat map illustrating rail height gradient in the device.

Figure S-3: Extent of device patterning capabilities on TCT PS.

Figure S-4: Images of scaled trapezoidal rail cross section.

Figure S-5: Schematic detailing model device dimensions.

Figure S-6: Design file images of injection-moldable Monorail Device.

Video S-1: Device workflow and platform function.

Video S-2-5: Significance of specific design features for successful SCF-driven patterning.

Video S-6-7: Performance of platform with multiple cell culture compatible hydrogels.

Table S-1: Optimized loading volumes for each device geometry.

Table S-2: CAD design files for each device geometry.

Derivation of theoretical model for conditions for flow in our platform

The pressure in the aqueous phase is generated by surface tension and can be evaluated using the Young-Laplace equation, where ΔP is the pressure difference across a curved air-liquid interface, γ is the interfacial tension, and R_1 and R_2 are the radii of curvature of the interface at a point on the interface in two orthogonal directions (e.g., horizontal and vertical).

The Laplace pressure difference (ΔP) at every interface is zero when the interface is flat ($R_1 = R_2 = \infty$). When the curvature of an interface is concave due to favorable wetting (i.e., contact angle $< 90^\circ$), the Laplace pressure difference becomes negative. Inversely, when the curvature is convex, the Laplace pressure difference becomes positive. Laplace pressure is a well-defined phenomenon that can be controlled experimentally and used to predict conditions for flow in our system.

Conditions for flow in an open channel have been derived in a general way by Berthier et al.¹ and are known as the spontaneous capillary flow (SCF) equation (in the case of a channel that has the same contact angle on all faces) or as the generalized Cassie angle equation (for the more general case when there are any number of contact angles along the surface of the channel). The current analytical models, however, assume that the pressure at the inlet of the open channel is negligible. The models allow prediction of the theoretical ability for SCF to occur. In order to refine the conditions for flow in our system, we added a pressure balance analysis between the surface tension-based pressures at the inlet and at the advancing fluid front (assuming the front exists).

The inlet of our system is a rectangular cross-section defined by the insert and the walls of the well plate. The liquid meniscus at the inlet is concave due to the wettability of the insert and well (contact angle $< 90^\circ$) and the interface will take the shape of a cylinder (as the channel cross-section is long (8.6 mm) and narrow (1 mm)). The radius of curvature along the long edge of the channel inlet is thus infinitely large, while the radius of curvature R_3 along the smaller edge of the inlet is uniquely characterized by two different contact angles with the device insert and the well plate, respectively (Figure S1). The pressure of the fluid at the inlet is written as:

$$\Delta P_{inlet} = \gamma \left(\frac{1}{R_3} \right) \quad (\text{Eq. 1})$$

The fluid front advancing under the plastic rail has a more complex geometry. The fluid front is described by a saddle point as the liquid is wetting the rail ceiling and well floor plastics (creating a concave fluid interface in the x-z plane) and is rounded from the top view as the channel does not have any side walls (the interface is convex in the x-y plane) (Figure S1). The pressure at the fluid front is described by Eq. 2, where R_1 is chosen to be the radius of curvature in the x-z plane, and R_2 is chosen as the radius of curvature in the x-y plane:

$$\Delta P_{front} = \gamma \left(\frac{1}{R_1} + \frac{1}{R_2} \right) \quad (\text{Eq. 2})$$

The condition for flow in our system requires the Laplace pressure of the inlet to be greater than the Laplace pressure at the fluid front in order to drive the fluid towards the area of lowest pressure:

$$\gamma\left(\frac{1}{R_3}\right) > \gamma\left(\frac{1}{R_1} + \frac{1}{R_2}\right) \quad (\text{Eq. 3})$$

Therefore, the limit of flow will occur when the two pressures are equal:

$$\gamma\left(\frac{1}{R_3}\right) = \gamma\left(\frac{1}{R_1} + \frac{1}{R_2}\right) \quad (\text{Eq. 4})$$

Or:

$$\frac{1}{R_1} + \frac{1}{R_2} - \frac{1}{R_3} = 0 \quad (\text{Eq. 5})$$

The radii of curvature in our system are governed by the physical aspect ratio of the channel, which includes the width w of the rail and the gap g_{front} between the rail and the well plate ($g_{\text{front}} = h$), the gap g_{inlet} between the insert and the well wall, and the contact angles of the fluid on the rail and the well plate surfaces.

We derived an equation for the radius of curvature of the fluid in the advancing filament in the x-z plane in function of the contact angles of the fluid on the well plate (θ_2), the contact angle of the fluid on the rail (θ_1), and the height of the rail (h). Using the geometric relations illustrated in Figure S1, we obtain:

$$R_1 = -\left(\frac{h}{\cos \theta_1 + \cos \theta_2}\right) \quad (\text{Eq. 6})$$

To assess the curvature of radius R_2 , we assume that the fluid is minimizing the surface energy, and thus assume that the interface is taking the shape of a large semi-circle of the same radius as the half-width of the rail.

We apply the same reasoning utilized to determine R_1 in Eq. 6 in order to derive R_3 , as a function of g_{inlet} , θ_2 , and θ_1 . Substitution of R_1 , R_2 , and R_3 into Equation 5 yields:

$$\frac{1}{-\left(\frac{h}{\cos \theta_1 + \cos \theta_2}\right)} + \frac{1}{\frac{w}{2}} - \frac{1}{\left(\frac{g_{\text{inlet}}}{\cos \theta_1 + \cos \theta_2}\right)} = 0 \quad (\text{Eq. 7})$$

Where w is the width of the rail, h is the height of the rail, and g_{inlet} is the space between the well and the device at the inlet in mm. Solving for h yields:

$$h = \frac{\cos \theta_1 + \cos \theta_2}{\frac{2}{w} + \frac{\cos \theta_1 + \cos \theta_2}{g_{\text{inlet}}}} \quad (\text{Eq. 8})$$

Equation 8 is graphed to give the boundary between the red and green shaded regions in Figure 2b, providing a model to predict when flow will occur in our system for devices based on the device dimensions.

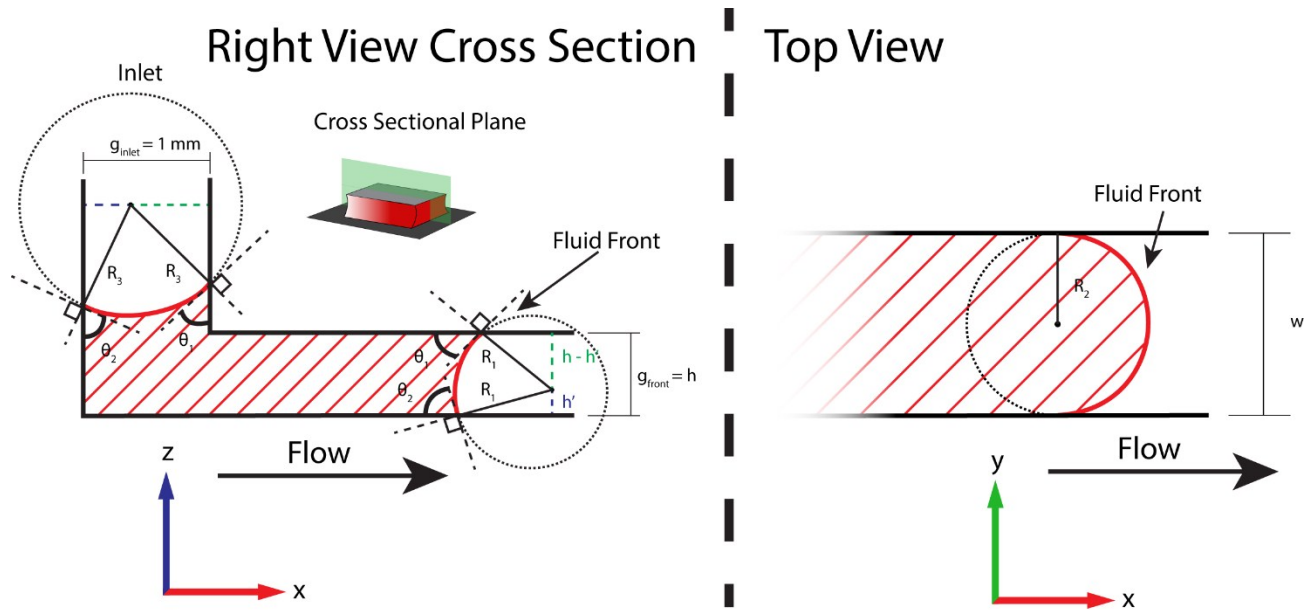


Figure S-1. Illustrations of radii of curvature for the calculation of Laplace pressure differences in our system. Perspectives demonstrate the radii of curvature (R), the contact angle between the liquid and the surface (θ), the height of the channel (h), the width of the channel (w), and the gap between the insert and the patterned surface (g).

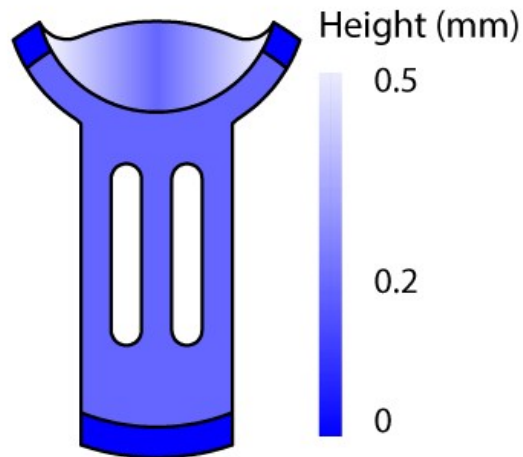


Figure S-2. Heat map illustrating the height of the rail above the well plate surface. Regions of the device with a lower height to width ratio are more favorable for spontaneous capillary flow (SCF), and tuning the height as shown enables controlled and reproducible hydrogel flow. The height gradient along the loading zone directs flow towards the middle of the flow path while feet (shown in dark blue, $h = 0$ mm) keep the patterning region off the surface.

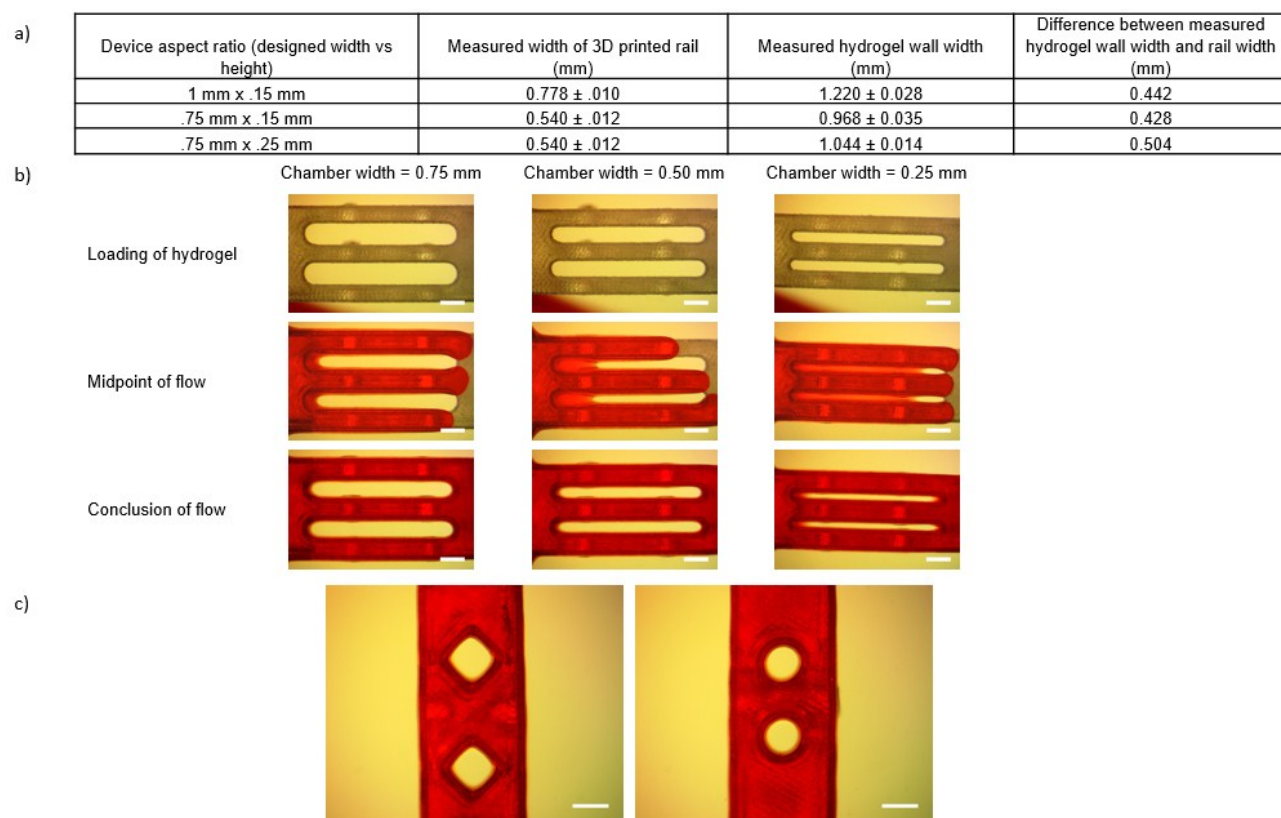


Figure S-3. Extent of device patterning capabilities on TCT PS. A) Extent of flooding along a rail. Devices were filled with matrigel dyed with red food dye and imaged from beneath ($n = 3$ devices). Data presented in the table represent the average width of the wall \pm SD for three different device aspect ratios. Height, in addition to width, influences the flooding of the chamber by the wall. B) Limit of culture chamber area due to flooding. Our platform enables fabrication of culture chambers down to a resolution of 0.25 mm width, below which we observed complete flooding of the culture chambers during the flow. At the conclusion of flow, the gel receded from the chamber leaving gel residue on the chamber floor. Images are representative of flow in $n = 3$ devices on TCT PS at different time points. Scale bar = 1 mm. C) Geometric patterning capabilities of our platforms. Scale bars = 1 mm.

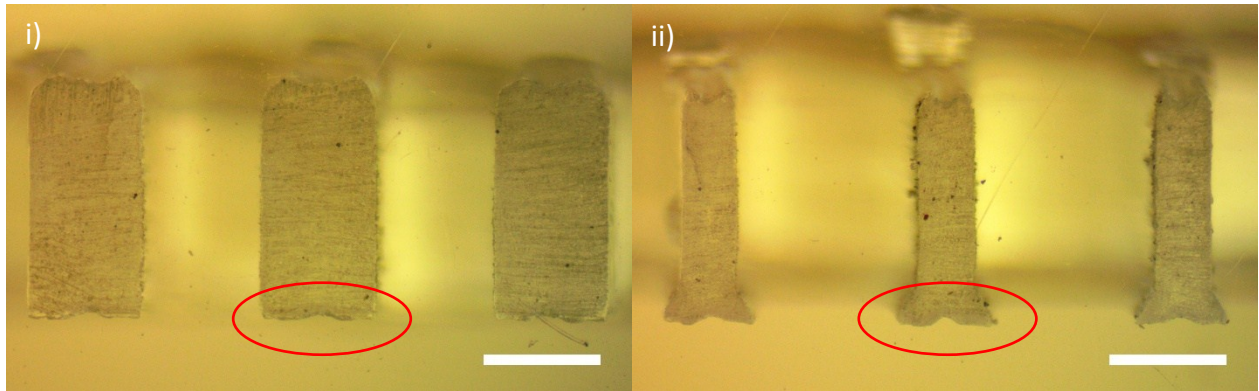


Figure S-4. Images represent the trapezoidal rail cross section. Cross sections presented here illustrate the rail without (i) and with (ii) a trapezoidal pinning feature at the scale used in each device. 3D-printed defects can be observed along the base of the rail, which were consistent throughout all devices. Scale bar = 1 mm.

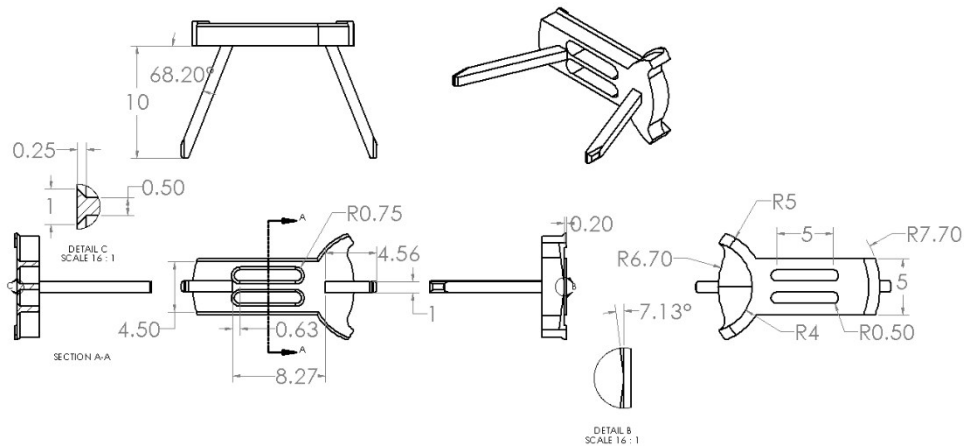


Figure S-5. Schematic diagrams illustrating the dimensions of our platform. All dimensions are in mm. CAD files are also included for all devices.

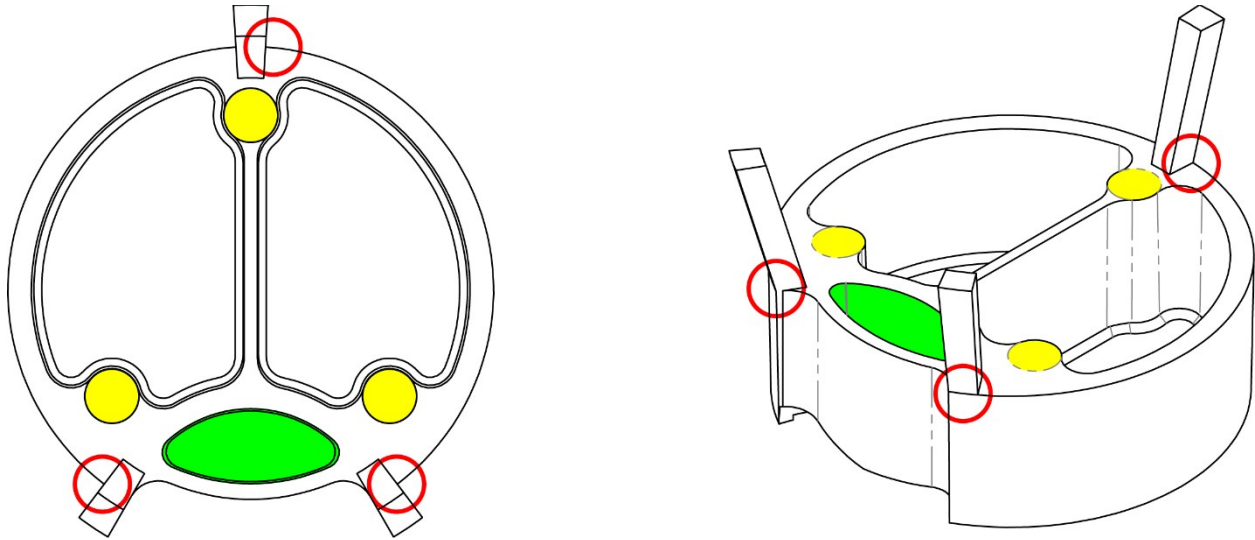


Figure S-6. Schematic images of an injection-moldable version of the Monorail Device. The Monorail design was modified for manufacturing by injection molding through the addition or modification of features of importance to the injection molding process. These features include: mold ejection zones (yellow) that provide an increased surface area for ejection pin/device contact; a cavity (green) to maintain a homogenous device thickness and avoid device deformation during cooling and setting steps; and re-positioned pressure struts (red) to avoid overhang, allowing fabrication with a two-piece mold. Further, the entire piece is drafted to a 1° angle to aid in device removal from the mold. The design file is included and listed in Table S2.

Video S-1. Platform setup and operation. Device is loaded with red-dyed matrigel and allowed to flow to completion along the rail, patterning the well-plate surface.

Video S2-5. Flow of red-dyed matrigel in two-chambered coculture devices in the presence or absence of design features. S2, control device with all design feature incorporated; S3, no controlled inlet; S4, no capillary sink; S5, no trapezoidal rail.

Video S6-7. Flow of alternative hydrogels in the Monorail Device to demonstrate compatibility with different materials. S6, flow of collagen I (4.17 mg/mL, 35 μ L, Corning Inc.); S7, flow of fibrinogen/thrombin solution to form fibrin (20 mg/mL fibrinogen, 2500 u/mg thrombin, 35 μ L, Sigma-Aldrich). Videos are representative of n = 3 replicates.

Table S-1. Optimized matrigel loading volumes associated with each device aspect ratio and geometry

Device	Height (mm)	Width (mm)	Loading Volume (μ L)
Figure 2b	0.15	0.50	25
	0.15	0.60	25
	0.15	0.75	20
	0.15	1.00	20
	0.25	0.50	35
	0.25	0.60	35
	0.25	0.75	30
	0.25	1.00	25
	0.35	0.50	35
	0.35	0.60	35
	0.35	0.75	30
	0.35	1.00	30
Figure 2c	0.25	1.00	25
Figure 3	0.20	1.00	25
Figure 4a	0.20	1.00 - 2.00	35
Figure 4b	0.20	1.00	85
Figure 5	0.20	1.00	40
Figure 6	0.20	1.00	50

Table S-2. CAD device design files

Device	CAD File
Figure 2	Single_Rail_Device.dwg
Figure 3 a/b	Two_Chamber_Device.dwg
Figure 3 c	Glass_Well_Single_Rail_Device.dwg
Figure 4 a	Coculture_Device.dwg
Figure 4 b	Diffusion_Test_Device.dwg
Figure 5	Morphology_Test_Device.sldprt
Figure 6a	Multiculture_Device.dwg
Figure 6b	Multiculture_Device_Peg.dwg

IM Device	InjectionMolding_MonorailDevice.sldprt
-----------	--

Reference:

1. J. Berthier, K.A. Brakke, E. Berthier, "Open Microfluidics". Wiley; 2016